Regimes of the Electron Diffusion Region in Magnetic Reconnection

A. Le, J. Egedal, O. Ohia, W. Daughton, H. Karimabadi, and V. S. Lukin

Regimes of the Electron Diffusion Region in Magnetic Reconnection

A. Le

Department of Physics, and Plasma Science and Fusion Center,

MIT, Cambridge, Massachusetts 02139, USA and

SciberQuest, Del Mar, CA 92014, USA

J. Egedal and O. Ohia

Department of Physics, and Plasma Science and Fusion Center,

MIT, Cambridge, Massachusetts 02139, USA

W. Daughton

Los Alamos National Laboratory, Los Alamos, New Mexico 87545, USA

H. Karimabadi

SciberQuest, Del Mar, CA 92014, USA

V. S. Lukin

Naval Research Laboratory, Washington, D.C. 20375, USA

Abstract

The electron diffusion region during magnetic reconnection lies in different regimes depending on the pressure anisotropy, which is regulated by the properties of thermal electron orbits. In kinetic simulations at the weakest guide fields, pitch angle mixing in velocity space causes the outflow electron pressure to become nearly isotropic. Above a threshold guide field that depends on a range of parameters, including the normalized electron pressure and the ion-to-electron mass ratio, electron pressure anisotropy develops in the exhaust and supports extended current layers. This new regime with electron current sheets extending to the system size is also reproduced by fluid simulations with an anisotropic closure for the electron pressure. It offers an explanation for recent spacecraft observations.

Magnetic reconnection, a rapid reconfiguration of the magnetic field embedded in a plasma, energizes particles in explosive events such as fusion experiment disruptions, solar coronal flares, and magnetospheric substorms [1]. A still unresolved question is how electron physics couples to the larger structure of the reconnecting plasma.

In collisionless regimes, such as most space plasmas, the collective electron dynamics is tied to the kinetic behavior of the individual particles. A variety of charged particle orbits are possible even in simplified, prescribed magnetic fields that qualitatively resemble reconnection geometries [2, 3]. Already in the linear phase of the tearing mode, three regimes have been identified depending on how strongly the electron orbits are magnetized [4]. Particle-in-cell (PIC) methods afford a numerical means of studying how the various classes of particle orbits, including meandering, chaotic, and magnetized adiabatic orbits, self-consistently feed back on magnetic reconnection. Here, we report on a series of PIC simulations with varying ion-to-electron mass ratio, guide magnetic field, and upstream normalized electron pressure. We find a number of regimes related to qualities of the electron orbits.

We identify a new regime that includes an electron current sheet extending to the simulated system size embedded in the reconnection exhaust. A fluid simulation that accounts for electron pressure anisotropy [5] reproduces the embedded current layer in larger simulation domains. The current layers form a basic feature of the electron diffusion region, taken here to mean where the electron frozen-in condition is violated. Magnetic dissipation need not occur in this so-called diffusion region, and it remains to be seen how the electron layers alter dissipation in regions with more restrictive definitions as in Ref. [7]. We note also that the layers may be unstable to secondary instabilities and thus profoundly influence the reconnection dynamics in 3D systems [6].

The new regime is a good candidate for the electron diffusion region inferred from Cluster spacecraft data collected in Earth's magnetosheath during reconnection [8]. And it resolves discrepancies between observation and simulation pointed out by Goldman *et al.* [9], in particular that previously identified current layers of unmagnetized electrons are shorter in simulations and are deflected by guide fields much weaker than the measured one. Additional spacecraft data may become available soon, as NASA's upcoming Magnetospheric Multiscale Mission has the express goal of taking high-resolution electron measurements.

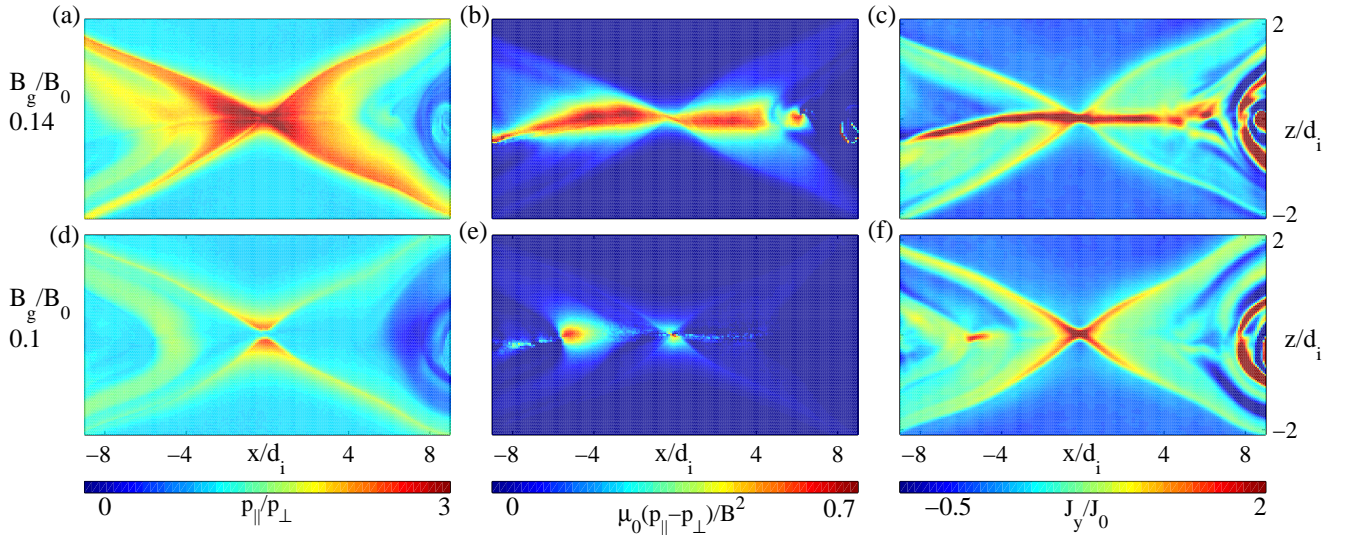We use three ion-to-electron mass ratios of $m_i/m_e = 100$, 400, and 1836 in simulations

FIG. 1: (a) Electron pressure anisotropy with $p_\parallel/p_\perp > 1$ extends into the exhaust with a guide field of $B_g/B_0 = 0.14$, (b) approaches the firehose threshold $\mu_0(p_\parallel - p_\perp)/B^2 = 1$, and (c) drives an out-of-plane current density J_y/J_0 ($J_0 = n_0 e v_{A0}$, where $v_{A0} = B_0/\sqrt{\mu_0 n_0 m_i}$). (d-f) The electrons are nearly isotropic for $B_g/B_0 = 0.1$. ($m_i/m_e = 1836$ and $\beta_{e\infty} \sim 0.09$.)

with the code VPIC [10]. Although the total reconnection rate is largely insensitive to the implemented mass ratio [11–13], we find other measurable quantities, including the current density profile and electron pressure anisotropy, strongly depend on this parameter. The initial conditions contain a Harris sheet with unperturbed magnetic field components $B_x = B_0 \tanh(z/\lambda)$ and $B_y = B_g$, where $\lambda = 0.5d_i$. The domain is $L_x \times L_z = 20d_i \times 20d_i$ ($40d_i \times 20d_i$ for $m_i/m_e = 100$) with no gradients in the y direction and open boundary conditions in the exhaust. For each mass ratio, the uniform guide field B_g is scanned over a range of values from $B_g/B_0 = 0$ to 0.8. The Harris sheet plasma parameters are characterized by $T_{i0}/T_{e0} = 5$ and $\omega_{pe}/\omega_{ce} = 2$, with $v_{the}/c = \sqrt{T_{e0}/m_e c^2} = 0.14$. The Harris sheet is superposed on a slightly cooler background with $T_{eb}/T_{e0} = 0.76$ and uniform density $n_b = 0.076$, 0.23, or $0.68n_0$ (n_0 is the peak Harris density). This yields an upstream $\beta_{e\infty} \sim 2\mu_0 n_b T_{eb}/B_0^2$ of ~ 0.01, 0.03, or 0.09 . The proton mass ratio runs employ a grid of 5120×5120 cells and $\sim 10^{10}$ numerical particles of each species.

For all sets of parameters, electric fields parallel to the magnetic field heat the inflow electron fluid according to known equations of state and produce electron pressure anisotropy with $p_\parallel \gg p_\perp$ [14, 15]. For sufficiently strong guide magnetic fields, the electron orbits remain
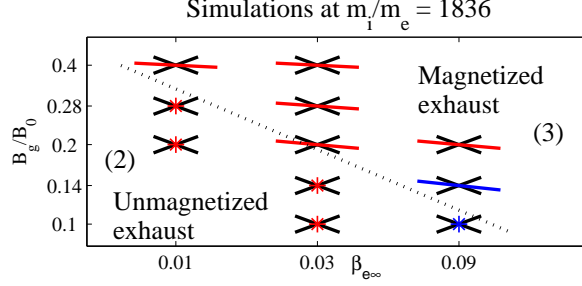
3

FIG. 2: Classification of simulation runs of varying upstream $\beta_{e\infty}$ and guide field B_g/B_0 at $m_i/m_e = 1836$. Symbols indicate the structure and length of the electron diffusion region. Runs marked in blue appear in Fig. 1, and numbers refer to regimes described below. Along the dashed curve, $K \sim 2.5$.

magnetized in the outflow and pressure anisotropy with $p_\parallel \gg p_\perp$ develops in the exhaust, as in the example in Fig. 1(a). A measure of the electron pressure anisotropy is how closely it approaches the firehose instability threshold, $p_\parallel - p_\perp = B^2/\mu_0$. The normalized anisotropy $\mu_0(p_\parallel - p_\perp)/B^2$ corresponding to Fig. 1(a) is plotted in Fig. 1(b), and it reaches $\gtrsim 0.7$ (the value 1 is the firehose threshold) along the center of the exhaust.

When the firehose condition is approached, we discover the regime that includes a system-length magnetized electron current layer. Although pressure anisotropy does not lead to magnetic dissipation on its own, the pressure tensor divergence breaks the electron frozen-in condition:

$$\mathbf{E} + \mathbf{u_e} \times \mathbf{B} \sim -\frac{1}{en_e}\nabla \cdot [(\mathbf{p}_\parallel - \mathbf{p}_\perp)\hat{\mathbf{b}}\hat{\mathbf{b}}], \tag{1}$$

and drives a current $\mathbf{J}_\perp \sim (p_\parallel - p_\perp)\mathbf{B} \times (\hat{\mathbf{b}} \cdot \nabla\hat{\mathbf{b}})/B^2$. The current flows across the magnetic field above the local $E \times B$ velocity in a narrow layer embedded in the exhaust [see Fig. 1(c)]. Following Refs. [16, 17], the firehose threshold may be expected to hold outside any quasi-1D current sheet with a normal component of magnetic field.

Adiabatic invariance of $\mu = v_\perp^2/2B$ requires $\rho_e/R_B \ll 1$ [3], where ρ_e is the electron Larmor radius and $R_B = |\hat{\mathbf{b}} \cdot \nabla\hat{\mathbf{b}}|^{-1}$ is the magnetic field line radius of curvature. For weak guide fields, this condition breaks in the center of the reconnection exhaust, and pitch angle mixing due to non-adiabatic particle orbits renders the exhaust pressure nearly isotropic [see the example in Fig. 1(d-f)].

The level of effective pitch angle diffusion is controlled by the ratio of R_B to the thermal

4

electron Larmor radius, which we find must be based on the total energy (rather than only the perpendicular energy) for unmagnetized or marginally magnetized electrons. The electrons are observed to be in a fully magnetized regime when $K \gtrsim 2.5$, where

$$K^2 \equiv min \left(\frac{R_B}{\rho_{\text{eff}}} \right), \tag{2}$$

$\rho_{\text{eff}} = \sqrt{m_e T_{\text{eff}}}/eB$, $T_{\text{eff}} = Tr(\mathbf{P_e})/(3n_e)$ is defined through the trace of the electron pressure tensor $\mathbf{P_e}$, and the minimum is taken along all relevant field lines. K thus generalizes the parameter $\kappa = \sqrt{R_{B,min}/\rho_{e,max}}$ introduced in Ref. [3]. As reconnection develops, ρ_{eff} becomes larger if the electrons gain energy. The energization is parametrized by $e\Phi_{\parallel}$, which is the maximum energy gained by electrons from the parallel electric field, and it has been shown to scale as $\Phi_{\parallel} \propto \beta_{e\infty}^{-1/2}$ in low $\beta_{e\infty}$ anti-parallel reconnection [17, 18]. Because the electrons reach higher energies at low $\beta_{e\infty}$, a stronger guide field is required to maintain a magnetized electron exhaust. Figure 2 classifies simulation runs at three values of $\beta_{e\infty}$ all at the proton mass ratio, and we find $K \sim 2.5$ along the boundary.

To relate the regimes of Fig. 2 to previous studies, Fig. 3 presents the results of a comprehensive scan in m_e/m_e and B_g/B_0 at a fixed $\beta_{e\infty} \sim 0.03$. Here, we identify four regimes based on the characteristics of the electron pressure and current profile. For weak or moderate guide fields, simulations with the same value of $(B_g/B_0)\sqrt{m_i/m_e}$ tend to be in the same regime. This follows if we assume that the electron orbits near the X line are similar for a fixed ratio ρ_{eg}/d_i of the electron gyroradius in the guide field $\rho_{eg} \propto 1/B_g$ and the ion scale $d_i \propto \sqrt{m_i}$ relevant to kinetic reconnection.

The table summarizes the traits of each regime:

Regime	Inner Jets	Anisotropic Exhaust	Embedded Layer	K
1	Y	N	N	$K \lesssim 1$
2	N	N	N	$1 \lesssim K \lesssim 2.5$
3	N	Y	Y	$2.5 \lesssim K$
4	N	Y	N	$2.5 \lesssim K$

An example of the out-of-plane current J_y from each regime is plotted on the right in Fig. 4 from simulations at the proton mass ratio $m_i/m_e = 1836$ for various guide fields B_g/B_0 (marked in blue in Fig. 3). The plots on the left in Fig. 4 are from runs with $m_i/m_e = 400$,

and they illustrate the differences at a reduced mass ratio. More detailed characteristics of each regime are as follows:

(1) In the anti-parallel regime at zero or low guide field, an unmagnetized electron jet flowing at nearly the electron thermal speed develops in the inner electron diffusion region [9, 13, 19, 20]. Note that the inner jets persist to much higher guide fields at reduced mass ratios. They form when the magnetic field is weak enough to allow thermal electrons to follow meandering orbits [21], which requires $K \lesssim 1$ [3]. The meandering motion leads to rather complicated local electron velocity distributions [22], but gross momentum balance of the current layer is regulated by the upstream pressure anisotropy [17, 22, 23].

(2) Above a certain guide field, inner electron jets do not form. As pointed out in Ref. [9], the guide field prevents electrons from meandering about the magnetic field reversal. We find this regime in the range $1 \lesssim K \lesssim 2.5$ characterized by chaotic electron orbits. In both the simulations of Ref. [9] and our simulations, guide fields of $B_g \lesssim 0.1B_0$ deflect the inner electron jets at the proton mass ratio [see Fig.4(e)]. In this weak guide field regime, the non-adiabatic electron orbits in the outflow render the exhaust electron pressure nearly isotropic.

(3) A window opens at $2.5 \lesssim K$ where the electrons are magnetized, yet the guide field is weak enough for the pressure anisotropy to approach the firehose condition. The new regime has a layer of anisotropy reaching $\mu_0(p_\parallel - p_\perp)/B^2 > 0.7$, which drives a current $\mathbf{J}_\perp \sim (p_\parallel - p_\perp)\mathbf{B} \times (\hat{\mathbf{b}} \cdot \nabla\hat{\mathbf{b}})/B^2$ across the magnetic field [see Fig. 4(d)]. These current layers are $\lesssim 10d_e$ wide, with a length of $\gtrsim 15d_i$ that is limited by the simulation domain size. Interestingly, they do not appear to be unstable to secondary island formation in our 2D simulations, likely because field-aligned current filaments cannot form in 2D. In addition, electron pressure anisotropy with $p_\parallel > p_\perp$ may suppress secondary tearing. Although the current layer is shorter in the run at $m_i/m_e = 400$ in Fig. 4(c), we classify it as marginally in regime (3) because the electrons are magnetized and electron pressure anisotropy greatly enhances the local current density.

Unlike the inner unmagnetized jets of regime (1), the embedded layers can be described within a fluid framework. In fact, they are reproduced in fluid simulations by including the equations of state for the anisotropic electron pressure [5]. The fluid code allows larger simulation domains than currently feasible in kinetic simulation, and an example of an embedded layer $\sim 25d_i$ long in a larger domain of $48d_i \times 24d_i$ is plotted in Fig. 4(i). Note
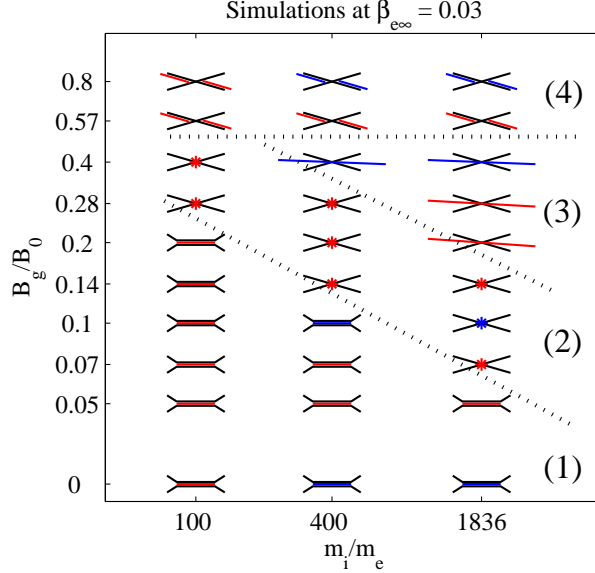
FIG. 3: Classification of simulation runs of varying mass ratio m_i/m_e and guide field B_g/B_0 at $\beta_{e\infty} = 0.03$. Symbols reflect the electron current structure in each of four regimes. (1) Inner electron jets ($\lesssim 100d_e$ long) and unmagnetized exhaust at $K \lesssim 1$. (2) No inner jets and an unmagnetized exhaust at $1 \lesssim K \lesssim 2.5$. (3) Magnetized current layer ($\gtrsim 15d_i$ long) at $2.5 \lesssim K$. (4) Magnetized exhaust without current layer. Runs marked in blue appear in Fig. 4.

that the fluid code employs $m_i/m_e = 400$, but it is comparatively insensitive to the mass ratio because the equations of state ensure that electron pressure anisotropy develops.

The long diffusion regions may be important in the magnetosphere, where the component of guide field is rarely weak enough to fully justify taking the anti-parallel limit. It likely explains the $> 60d_i$ long diffusion region observed by Cluster [8] in a plasma with $\beta_{e\infty} \sim 0.1$ and a guide field of $B_g \sim 0.15B_0$ [parameters close to those in Figs. 1(a-c)] . As noted in Ref. [9] and confirmed here, at $m_i/m_e = 1836$ the inner jet of the anti-parallel regime (1) is too short ($\sim 1d_i$) and a guide field of $B_g \sim 0.15B_0$ prevents this type of jet from forming. We find, however, that the 15% guide field is strong enough for the Cluster event to be in regime (3) characterized by a magnetized layer embedded in the exhaust.

(4) The electron orbits are magnetized, and they are not qualitatively different from those of regime (3). At high values of B_g, however, the electron pressure cannot compete with the tension of the guide field to approach the firehose condition. An embedded current layer does not form, and the current tends to peak only near the pair of diagonally opposed
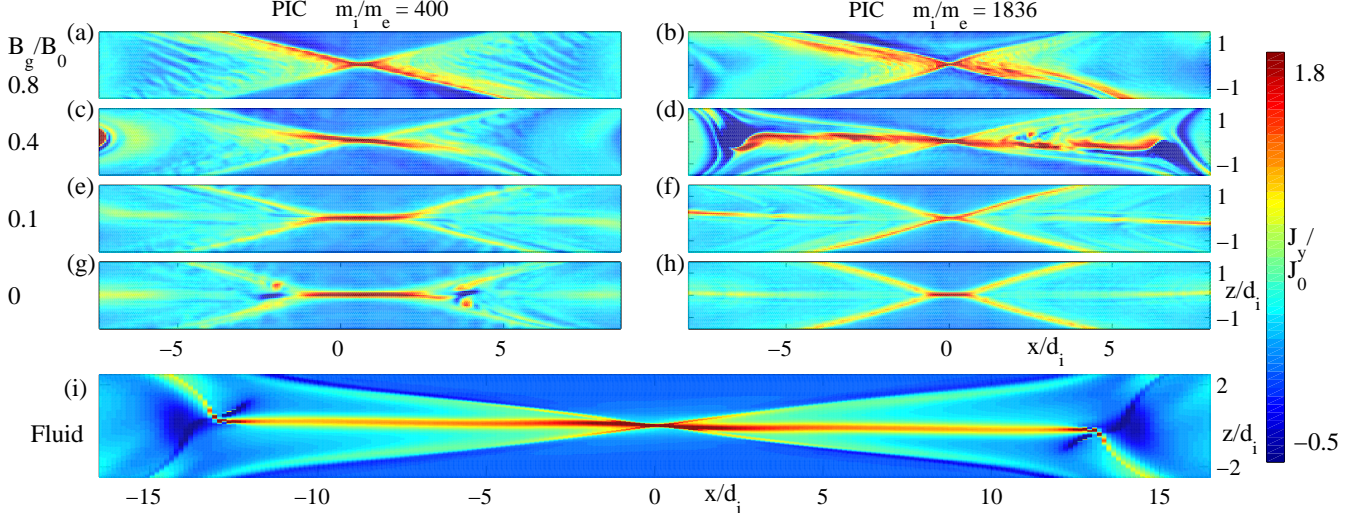
7

FIG. 4: J_y/J_0 with guide fields B_g/B_0 of (a,b) 0.8, (c,d) 0.4, (e,f) 0.1, and (g,h) 0 at time $t\omega_{ci} = 22.5$ from PIC runs with mass ratios of $m_i/m_e = 400$ and 1836 and $\beta_{e\infty} = 0.03$. (i) J_y/J_0 at time $t\omega_{ci} = 106$ from a larger ($48d_i \times 24d_i$) two-fluid simulation based on the HiFi code [24] including the electron pressure anisotropy, initially in a force-free configuration with $\beta_{e\infty} = 0.03$ and $B_g/B_0 = 0.28$.

separator field lines where the density is enhanced. For our $\beta_{e\infty} \sim 0.03$ runs, this occurs at $B_g/B_0 \sim 0.57$.

In summary, a new series of kinetic simulations demonstrate that currents and magnetic fields that develop during reconnection fall into different regimes depending on the guide field strength, the electron $\beta_{e\infty}$, and the implemented mass ratio. These results underscore the complexity of direct comparison of spacecraft data to simulation, which often must employ some unrealistic parameters and rely on extrapolation. Notably, a new regime with an extended embedded electron diffusion region is present in our simulations for an interval of guide fields that becomes wider as m_i/m_e increases and is most significant in our runs at the real proton-to-electron ratio.

[1] E. Priest and T. Forbes, *Magnetic Reconnection* (Cambridge University Press, 2000).

[2] T. Speiser, J. Geophys. Res. **70**, 4219 (1965).

[3] J. Buchner and L. Zelenyi, J. Geophys. Res. **94**, 11821 (1989).

[4] W. Daughton and H. Karimabadi, J. Geophys. Res. **110**, A03217 (2005).

[5] O. Ohia, J. Egedal, V. S. Lukin, W. Daughton, and A. Le, Phys. Rev. Lett. **109**, 115004 (2012).

[6] W. Daughton, V. Roytershteyn, H. Karimabadi, L. Yin, B. J. Albright, B. Bergen, and K. J. Bowers, Nature Physics **7**, 539 (2011).

[7] S. Zenitani, M. Hesse, A. Klimas, and M. Kuznetsova, Phys. Rev. Lett. **106**, 195003 (2011).

[8] T. D. Phan, J. F. Drake, M. A. Shay, F. S. Mozer, and J. P. Eastwood, Phys. Rev. Lett. **99** (2007) and private communication.

[9] M. V. Goldman, G. Lapenta, D. L. Newman, S. Markidis, and H. Che, Phys. Rev. Lett. **107**, 135001 (2011).

[10] K. J. Bowers, B. J. Albright, L. Yin, B. Bergen, and T. J. T. Kwan, Physics of Plasmas **15**, 055703 (2008).

[11] M. Hesse, K. Schindler, J. Birn, and M. Kuznetsova, Physics of Plasmas **6**, 1781 (1999).

[12] M. Swisdak, J. F. Drake, M. A. Shay, and J. G. McIlhargey, Journal of Geophysical Research (Space Physics) **110**, A05210 (2005).

[13] M. A. Shay, J. F. Drake, and M. Swisdak, Phys. Rev. Lett. **99** (2007).

[14] J. Egedal, W. Fox, N. Katz, M. Porkolab, M. Oieroset, R. P. Lin, W. Daughton, and D. J. F., J. Geophys. Res. **113**, A12207 (2008).

[15] A. Le, J. Egedal, W. Daughton, W. Fox, and N. Katz, Phys. Rev. Lett. **102**, 085001 (2009).

[16] S. W. H. Cowley, Planetary and Space Science **26**, 1037 (1978).

[17] A. Le, J. Egedal, W. Daughton, J. F. Drake, W. Fox, and N. Katz, Geophys. Res. Lett. **37**, L03106 (2010).

[18] J. Egedal, W. Daughton, and A. Le, Nature Phys. **8**, 321 (2012).

[19] W. Daughton, J. Scudder, and H. Karimabadi, Phys. Plasmas **13**, 072101 (2006).

[20] H. Karimabadi, W. Daughton, and J. Scudder, Geophys. Res. Lett. **34**, L13104 (2007).

[21] A. Ishizawa, R. Horiuchi, and H. Ohtani, Physics of Plasmas **11**, 3579 (2004).

[22] J. Ng, J. Egedal, A. Le, W. Daughton, and L. J. Chen, Phys. Rev. Lett. **106** (2011).

[23] M. Hesse, S. Zenitani, and A. Klimas, Phys. Plasmas **15**, 112102 (pages 5) (2008).

[24] V. S. Lukin and M. G. Linton, Nonl. Proc. Geophys. **18**, 871 (2011).